

# Microtheory of Scintillation in Crystalline Materials

Andrey N. Vasil'ev<sup>(✉)</sup>

Skobeltsyn Institute of Nuclear Physics, Lomonosov Moscow State University,  
Leninskie Gory, 1(2), 119991 Moscow, Russia  
anv@sinp.msu.ru

**Abstract.** The review of the processes in solid state scintillators is presented. All steps of the transformation of energy in scintillators (production of secondary electronic excitations, thermalization, migration and recombination, photon emission) are observed. The processes at these steps are characterized by quite different spatial and time scales. These scales differs for various classes of scintillators, depending on electron structure of conduction and valence bands, energy position of core levels, phonon spectrum, presence of activators and dopants. Therefore the microscopic structure of electronically and vibrationally excited regions is material dependent. In general this structure is characterized by high non-homogeneity. For instance, in crystals consisted from heavy ions with several low-energy core bands the effect of the clusterization of secondary electronic excitations plays important role in formation of new emission centers. We discuss the estimation of the scintillation yield, non-proportionality, energy resolution and decay characteristics based on the analysis of elementary processes in scintillators.

## 1 Introduction

Scintillation is a complex optical response of the condensed matter on an ionizing particle or a  $\gamma$ -quantum. These particles produce big number of electronic excitations which passes through several transformations and interactions and result in emission of a number of photons with energy corresponding to visible or near ultraviolet region. An ideal scintillator generates fast response with exponential decay, the number of photons is proportional to the energy deposited by the ionizing particle in the scintillator volume. Unfortunately this ideal scintillator does not exist. The relative yield of the scintillator depends on the type of ionizing particle and its energy, whereas the scintillation kinetics is typically far from monoexponential and shows either rising time and long components, the ratio between which also depends on the type and energy of the ionizing particle. The dependence of scintillator yield on the ionizing particle energy was studied since 60th (see e.g. [1, 2] and references in [3]). Nevertheless, the well-known formula used for estimation of the scintillation energy yield  $Y(E)$  (ratio of the number of emitted photons to energy of ionizing particle  $E$ ),  $Y(E) = \frac{1}{\beta E_g} SQ$  [4], supposes that the number of photons is proportional to  $E$ . All three factors corresponding to different stages of energy relaxation (namely, cascade which is described

by the mean energy cost of an electron–hole pair  $\beta E_g$ , transfer stage with efficiency  $S$  and emission efficiency of the radiation center  $Q$ ). Here  $E_g$  is the forbidden gap of the crystal,  $\beta \approx 1.5-3$ .

The problem of the dependence of the scintillation energy yield on the energy of ionizing particle became again under intense investigation in 90th [5–8]. This period is characterized by separation between energy dependencies for electron and photon ionization, and by proposition of the method of Compton coincidence technique [9, 10]. This method allows to study scintillation excited by an electron with fixed energy produced by Compton scattering in the interior of the crystal, thus eliminating all near-surface effects typical for excitation by electrons from the gun. This technique was further developed in 2000th in SLYNCI experiment [11, 12] and experiments carried out by the group of Moszyński [13]. Study of the dependence of scintillator yield on photon energy in low-energy region below few tens of keV was performed using so-called “K-dip” spectroscopy with synchrotron radiation by the group of Dorenbos [14–16], and for lower energies (up to 1 keV) in [17]. At the same time several theoretical approaches were developed for explanation of the non-proportionality in different classes of scintillating materials [18–23].

During recent years both theoretical and experimental studies of the scintillation non-proportionality problem were performed. We can mention phenomenological study of this effect and deterioration of scintillator energy resolution [24–27]. The connection between non-proportionality and energy resolution is not straightforward—there are some additional factors which deteriorate energy resolution, like excitation cluster formation [28, 29] and very low-energy (below 200 eV) non-proportionality [30].

The theoretical investigations typically describes only a part of processes involving in overall scintillation mechanism. Initial stages of interacting of ionizing particle with matter generally supposed to be well-known and described by simplified Bethe equation which is valid for electron energies above 1 keV. This approach does not take into account fluctuations of the scattering events (like Landau fluctuations which describe the fluctuations of the energy losses along the track). More accurate simulation of the primarily interaction of the ionizing particle with media can be made using different Monte-Carlo approaches like GEANT4 [31, 32] or NWEGRIM code resulting in generation of electron–hole pairs in space [33] and in energy [34, 35].

The second stage involving thermalization and diffusion of electrons and holes is mainly due to electron–phonon interaction. Length of thermalization can be estimated by simplified approach like in [28, 29, 36] or even experimentally estimated using the analysis of decay kinetics under synchrotron radiation VUV excitation [37]. An example of much more elaborated ab initio calculation of electron–phonon interaction can be found in [38]. The mobility of thermalized and hot charge carriers depends on the effective masses of low energy carriers which can be estimated using numerous band structure calculations [39–41] and properties of energy branches at higher energies, like group velocities of hot carriers. It is shown in [42] that the group velocity and therefore mobility of hot electrons is much less than that estimated for simple parabolic band model. An approach for estimation of spread of hot carriers from the points of their generation and their drift after thermalization in electric fields arisen from

separation of electrons and holes in cylindrical geometry was developed in [43–47]. We can mention another approaches for describing of this stage, for instance the usage of dynamical structure factor formalism [48] and balance equation approach describing the energy exchange in a hot bipolar plasma of electrons/holes and phonons [49]. We also should mention a successful development of techniques for simulation by the group from Pacific North-West National Laboratory (PNNL, WA, USA) with the collaborators. They develop a set of tools including calculation of elementary cross-sections and momentum-dependent energy loss functions [50], high-energy Monte-Carlo simulation of the cascade [33–35], simulation of the thermalization and finally package for kinetic Monte Carlo simulation of the last stage involving recombination and luminescence [51, 52]. Unfortunately these calculations are hardly scalable to high energies of ionizing particles and are very specific for different materials, so simplified approaches could be useful also.

Generally speaking, non-linear effects typical to scintillators can be observed under other types of excitation, like laser excitation. In this case the spatial distribution of excitations is also non-uniform, but can be controlled by the modification of laser spot dimensions and is influenced by the media absorption coefficient. The excited region is created by absorption of many laser photons (in contrary with scintillation event). If the duration of laser pulse is short enough (femtosecond lasers are preferable), these excitations are created about simultaneously like in a track of ionizing particle. A convenient way for control of the distribution is the defocusing of the laser spot which conserves the total number of excitations. The intensity of emission and decay kinetics occur to non-linear depend on the concentration of initial excitations. Thus such experiments [53–55] provide us with the information about interaction of carriers in different time domains. For instance, long-time dependence of the decay kinetics gives us the information about dipole-dipole quenching of luminescence [53, 54], and the dependence of integrated signal on the excitation density, about the quenching processes at initial stages of relaxation (like Auger recombination of carriers) [55]. These parameters are typically simulated by the usage of a set of kinetic (or rate) equations for all types of involved electronic excitations [43, 46, 47, 56, 57]. Such sets of equations are used to be solved in spatially uniform case. The averaging of the solutions over the excitation density distribution allows to obtain the integral result for excitation density dependence of total emission yield and decay kinetics [53, 54].

## 2 Interaction of Charged Particle with Media

Two stages of relaxation of energy—Cascade and Thermalization—are directly determined by the interaction of a charge of the ionizing particle with media. Here we have to remind some formulas from classical electrodynamics and to discuss how to pass to quantum approach. During the passage of a particle with charge  $Ze$  and velocity  $\mathbf{v}$  through the media with complex dielectric permittivity  $\tilde{\epsilon}(\omega, \mathbf{q})$  it produces alternating electric fields in the media. These spatial Fourier components of scalar potential  $\varphi(\mathbf{r}, t)$  and vector-potential  $\mathbf{A}(\mathbf{r}, t)$  can be calculated using Lienard–Wiechert formulas [58, 59]

$$\begin{aligned}\tilde{\mathbf{A}}_{\mathbf{q}}(t) &= \frac{Ze\mathbf{v}}{\varepsilon_0 c^2 \left( q^2 - (\mathbf{q}\mathbf{v})^2 \tilde{\varepsilon}(\mathbf{q}\mathbf{v}, \mathbf{q}) / c^2 \right)} e^{-i\mathbf{q}\mathbf{v}t}, \\ \tilde{\varphi}_{\mathbf{q}}(t) &= \frac{Ze}{\varepsilon_0 \varepsilon(\mathbf{q}\mathbf{v}, \mathbf{q}) \left( q^2 - (\mathbf{q}\mathbf{v})^2 \tilde{\varepsilon}(\mathbf{q}\mathbf{v}, \mathbf{q}) / c^2 \right)} e^{-i\mathbf{q}\mathbf{v}t}.\end{aligned}\quad (1)$$

Here  $\mathbf{q}$  is the wave vector. Using the relation  $\tilde{\mathbf{E}}_{\mathbf{q}} = i\omega\tilde{\mathbf{A}}_{\mathbf{q}} - i\mathbf{q}\tilde{\varphi}_{\mathbf{q}}$ , one can calculate Fourier components of the electric field

$$\tilde{\mathbf{E}}_{\mathbf{q}}(t) = \frac{Ze}{\varepsilon_0 \tilde{\varepsilon}(\mathbf{q}\mathbf{v}, \mathbf{q}) \left( q^2 - (\mathbf{q}\mathbf{v})^2 \tilde{\varepsilon}(\mathbf{q}\mathbf{v}, \mathbf{q}) / c^2 \right)} \left( \frac{i\mathbf{v}(\mathbf{q}\mathbf{v})\tilde{\varepsilon}(\mathbf{q}\mathbf{v}, \mathbf{q})}{c^2} - i\mathbf{q} \right) e^{-i\mathbf{q}\mathbf{v}t}. \quad (2)$$

Taking the reverse Fourier transformation, after some algebraic manipulations one can calculate the spatial and temporal dependence of the induced electric field

$$\begin{aligned}\mathbf{E}(\mathbf{r}, t) &= \frac{1}{(2\pi)^3} \int d^3q \tilde{\mathbf{E}}_{\mathbf{q}}(t) e^{i\mathbf{q}\mathbf{r}} \\ &= \frac{-iZe}{(2\pi)^3 \varepsilon_0} \int_{-\infty}^{\infty} d\omega \int d^3q \frac{1}{q^2} e^{i\mathbf{q}\mathbf{r} - i\omega t} \delta(\omega - \mathbf{q}\mathbf{v}) \left( \frac{\mathbf{q}}{\tilde{\varepsilon}(\omega, \mathbf{q})} + \frac{q^2 \mathbf{v} - \omega \mathbf{q}}{\omega(\tilde{\varepsilon}(\omega, \mathbf{q}) - q^2 c^2 / \omega^2)} \right).\end{aligned}\quad (3)$$

Electric field component along the ionizing particle velocity equals to

$$E_{\parallel}(\mathbf{r}, t) = \frac{-iZe}{(2\pi)^3 \varepsilon_0 v} \int_{-\infty}^{\infty} d\omega \int d^3q \frac{1}{q^2} e^{i\mathbf{q}\mathbf{r} - i\omega t} \delta(\omega - \mathbf{q}\mathbf{v}) \left( \frac{\omega}{\tilde{\varepsilon}(\omega, \mathbf{q})} + \frac{q^2 v^2 - \omega^2}{\omega(\tilde{\varepsilon}(\omega, \mathbf{q}) - q^2 c^2 / \omega^2)} \right), \quad (4)$$

and electric field component perpendicular to the particle velocity equals to

$$E_{\perp}(\mathbf{r}, t) = -\frac{iZe}{(2\pi)^3 \varepsilon_0 v^2} \int_{-\infty}^{\infty} d\omega \int d^3q \frac{v^2 \mathbf{q} - \omega \mathbf{v}}{\tilde{\varepsilon}(\omega, \mathbf{q}) (q^2 - \omega^2 \tilde{\varepsilon}(\omega, \mathbf{q}) / c^2)} e^{i\mathbf{q}\mathbf{r} - i\omega t} \delta(\omega - \mathbf{q}\mathbf{v}). \quad (5)$$

Taking the cylindrical coordinate system with axis  $z$  along the velocity and using the relation  $\tilde{\varepsilon}(-\omega, \mathbf{q}) = \tilde{\varepsilon}^*(\omega, \mathbf{q})$  into account, one can pass to integration over only positive frequencies:

$$E_{\parallel}(r_{\parallel}, r_{\perp}, t) = -\frac{Ze}{2\pi^2\epsilon_0 v^2} \int_0^{\infty} \omega d\omega \int_{\omega/v}^{\infty} \frac{dq}{q} J_0\left(r_{\perp} \sqrt{q^2 - \frac{\omega^2}{v^2}}\right) \times \text{Im} \left[ e^{i\omega(r_{\parallel}/v - t)} \left( -\frac{1}{\tilde{\epsilon}(\omega, q)} - \frac{\left(\frac{q^2 v^2}{\omega^2} - 1\right)}{\tilde{\epsilon}(\omega, q) - \frac{q^2 c^2}{\omega^2}} \right) \right] \quad (6)$$

$$E_{\perp}(r_{\parallel}, r_{\perp}, t) = -\frac{Ze}{2\pi^2\epsilon_0 v^2} \int_0^{\infty} \omega d\omega \int_{\omega/v}^{\infty} \frac{dq}{q} \sqrt{\frac{q^2 v^2}{\omega^2} - 1} J_1\left(r_{\perp} \sqrt{q^2 - \frac{\omega^2}{v^2}}\right) \times \text{Re} \left[ e^{i\omega(r_{\parallel}/v - t)} \left( -\frac{1}{\tilde{\epsilon}(\omega, q)} + \frac{1}{\tilde{\epsilon}(\omega, q) - \frac{q^2 c^2}{\omega^2}} \right) \right] \quad (7)$$

The force  $F = ZeE_{\parallel}(vt, 0, t)$  acting on the ionizing particle from this induced fields can be calculated by substitution the trajectory equations  $r_{\perp} = 0, r_{\parallel} = vt$  into the expression for  $E_{\parallel}(r_{\parallel}, r_{\perp}, t)$ . Multiplying this force by the particle velocity  $W = Fv$ , one can obtain the power of energy losses due to interaction with media, and therefore the energy losses per unit traveling distance (stopping power) can be expressed in classical approach as

$$\frac{dE}{dx} = -\frac{Z^2 e^2}{2\pi^2 \epsilon_0 v^2} \int_0^{\infty} \omega d\omega \int_{\omega/v}^{\infty} \frac{dq}{q} \times \left( \text{Im} \left( -\frac{1}{\tilde{\epsilon}(\omega, q)} \right) + \left( \frac{q^2 v^2}{\omega^2} - 1 \right) \text{Im} \left( -\frac{1}{\tilde{\epsilon}(\omega, q) - \frac{q^2 c^2}{\omega^2}} \right) \right) \quad (8)$$

Quantum mechanics introduces some important corrections in this formula. This formula can be treated as energy losses in scattering process, in which ionizing particle with kinetic energy  $E$  is scattered with production of secondary electronic excitation with energy  $\hbar\omega$  and momentum  $\hbar\mathbf{q}$ . First of all, scattering kinematics restricts the integration regions. The maximal transferred energy is limited by the kinetic energy of the primary particle, whereas the transferred momentum is limited by momentum and energy conservation laws. For instance, for electrons with kinetic energy above tens of electronvolts one can use parabolic (or relativistic) energy dispersion law with electron free mass. In this case the stopping power (Eq. 8) can be written as

$$-\frac{dE}{dx} = \frac{2Z^2}{\pi a_0 m_0 v^2(E)} \int_0^E \hbar\omega d(\hbar\omega) \int_{q_{\min}}^{q_{\max}} \frac{dq}{q} \text{Im} \left[ -\frac{1}{\tilde{\epsilon}(\omega, q)} - \frac{v^2(E)q^2/\omega^2 - 1}{\tilde{\epsilon}(\omega, q) - c^2 q^2/\omega^2} \right] \quad (9)$$

$$q_{\min}^{\max} = \frac{1}{\hbar c} \left( \sqrt{E(E + 2Mc^2)} \pm \sqrt{(E - \hbar\omega)(E - \hbar\omega + 2Mc^2)} \right). \quad (10)$$

Here we use relativistic expression for velocity,  $v = c\sqrt{E(E + 2Mc^2)} / (E + Mc^2)$ ,  $M$  is the ionizing particle mass,  $a_0 = \frac{4\pi\epsilon_0\hbar^2}{m_0e^2}$  is Bohr radius for hydrogen. In non-relativistic case this formula is simplified to  $v = \sqrt{2E/M}$ . The lower limit  $q_{\min}$  of integration over the momentum equals to  $q_{\min} = \omega(E + Mc^2) / (c\sqrt{E(E + 2Mc^2)}) = \omega/v$  in accordance with Eq. 8. The same limits of integration over  $q$  and  $\hbar\omega$  should be applied for Eqs. 6 and 7.

The second important consequence from the quantum nature of energy losses is that they can be treated as a sequence of individual scatterings, with mean free path between scatterings calculated by the formula

$$\frac{1}{\lambda(E)} = \frac{2Z^2}{\pi a_0 m_0 v^2(E)} \int_0^E d(\hbar\omega) \int_{q_{\min}}^{q_{\max}} \frac{dq}{q} \text{Im} \left[ -\frac{1}{\tilde{\epsilon}(\omega, q)} - \frac{v^2(E)q^2/\omega^2 - 1}{\tilde{\epsilon}(\omega, q) - c^2q^2/\omega^2} \right] \quad (11)$$

which differs from Eq. 9 by division of the integrand by the energy of scattered quantum,  $\hbar\omega$ . The mean inverse time between individual scatterings equals to  $\tau^{-1}(E) = v(E)/\lambda(E)$  and has the same structure as Eq. 11.

There are a lot of corrections to formulas Eqs. 9 and 11, but the main structure of it remains unchanged. The core of this formula is the complex dielectric permittivity function  $\tilde{\epsilon}(\omega, \mathbf{q})$ , the structure of which will be discussed below. There are some of the corrections and details of this formula:

1. The corrections includes the account of indistinguishability of primary and secondary electrons (if the ionizing particle is electron) and some relativistic corrections.
2. Equation 9 is correct for uniform media. Crystals have translational symmetry with three lattice constant vectors, for this case the transferred wave vector  $\mathbf{q}$  lies within the first Brillouine zone, and the dielectric permittivity becomes the multidimensional tensor  $\tilde{\epsilon}_{ij, \mathbf{G}\mathbf{G}'}(\omega, \mathbf{q})$  ( $i, j = x, y, z$ ,  $\mathbf{G}$  and  $\mathbf{G}'$  are the vectors in the reciprocal space,  $\mathbf{G} = n_1\mathbf{b}_1 + n_2\mathbf{b}_2 + n_3\mathbf{b}_3$ ,  $n_\alpha$  are integers). The calculation of this tensor is a very hard problem, some attempts are made in [50]. Nevertheless, the main features of the production of secondary excitations can be done using the uniform media approximation. In this case we disregard some effects like channeling of the particles.
3. The crystalline structure of dielectric permittivity is most important for interaction of low energy electrons with energy below few tens of electronvolts. Another problem to describe this low-energy region is the complicated energy dispersion law for electrons and holes. The energy of carriers is described as many branches  $E_s(\mathbf{k})$  where wave-vector changes within the first Brillouine zone, and each scattering process can involve several branches. The velocity of carrier is defined as  $\mathbf{v}_s(\mathbf{k}) = \hbar^{-1} \partial E_s(\mathbf{k}) / \partial \mathbf{k}$ . The difference between the group velocities averaged over

Brillouine zone for definite kinetic energy  $E$  and parabolic band approximation was studied in details for some scintillating crystals in [42]. Another example is the estimation of scattering probability near the inelastic scattering threshold for multiple-parabolic-band model [60], which is the example of complicated energy dispersion law.

4. Only near the bottom of the conduction band and near the top of the valence band one can use effective mass approximation with mass  $m_{e,h}^*$ . This approximation is valid only in narrow energy region (typically less than 1 eV), and even in this case the crystal is anisotropic and the effective mass becomes a tensor. Nevertheless, this approximation is widely used for the description of interaction of carriers with phonons, and Eqs. 8 and 9 are widely used again. This case will be discussed below in details.

The structure of the stopping power described by Eq. 9 shows that energy losses can be treated as emission of virtual photons with energies  $\hbar\omega$  from 0 to the energy of ionizing particle  $E$ , and the probability of what energy could be emitted per unit length is defined by the integrand in the integral for inverse mean free path (Eq. 11). There are two terms in this integrand, the former is connected with emission of longitudinal virtual photons (the term with so called “energy loss function”  $\text{Im}(-\tilde{\epsilon}^{-1}(\omega, \mathbf{q}))$ ), the latter is defined by emission of virtual and real photons proportional to  $\text{Im}\left(-(\tilde{\epsilon}(\omega, q) - q^2 c^2 / \omega^2)^{-1}\right)$ . The simplest interpretation of the former term is the production of plasmons, since the equation for plasmons is  $\tilde{\epsilon}(\omega, \mathbf{q}) = 0$  and therefore energy loss function should have a prominent peak for plasmon frequency. The latter term includes the emission of real transversal photons, since the dispersion law for them is  $q = \omega \tilde{n}(\omega, q) / c$ ,  $\tilde{n}(\omega, q) = \sqrt{\tilde{\epsilon}(\omega, q)}$  is the complex refraction index. When  $\hbar\omega$  corresponds to the transparency region of the matter, this term describes Cherenkov radiation. But for most non-relativistic cases this term can be neglected, so below we pay attention mainly on the term with energy loss function  $\text{Im}(-\tilde{\epsilon}^{-1}(\omega, \mathbf{q}))$ .

The energy loss function is non-zero in all regions of photon energy which can be absorbed by the media. For insulators it includes (i) fundamental absorption region  $\hbar\omega > E_{ex}$  where  $E_{ex} < E_g$  is the lowest energy of excitons,  $E_g$  is the forbidden gap energy. This region corresponds to the creation of different types of electronic excitations in insulator by an ionizing particle: excitons, electron–hole pairs and core level excitations; (ii) possible absorption bands in the transparency region (where the transfer results in excited or ionized states of defects); and (iii) infrared absorption region with  $\hbar\omega < \hbar\Omega_{\max}$  where phonons are emitted. Here  $\Omega_{\max}$  is the maximal frequency of phonons (which is about longitudinal optical phonon frequency  $\Omega_{LO}$ ). The integral in Eq. 9 is taken over all energies including phonon energy region from zero to the energy of ionizing particle. We can separate these two types of energy losses (neglecting the energy losses due to impact excitation/ionization of defects). The stopping power due to emission of electronic excitations can be written in non-relativistic case as

$$\left(-\frac{dE}{dx}\right)_{e-h} = \frac{1}{\pi a_0 E} \int_{E_{ex}}^E \hbar \omega d(\hbar \omega) \int_{q_{\min}}^{q_{\max}} \frac{dq}{q} \operatorname{Im} \left( -\frac{1}{\varepsilon(\hbar \omega, q)} \right), \quad (12)$$

The limits of integration over  $q$  are

$$q_{\min}^{\max} = \frac{\sqrt{2m_0}}{\hbar} \left( \sqrt{E} \pm \sqrt{E - \hbar \omega} \right) \quad (13)$$

Here we discuss electrons as ionizing particles, since electrons are produced during the cascade. The energy losses for a primary ionizing particle different from an electron are larger by a factor  $Z^2 M/m_0$  for the same energy, and expressions for limits of integration over  $q$  includes  $\sqrt{M}$  instead of  $\sqrt{m_0}$ . If we neglect the momentum dependence of dielectric function,  $\operatorname{Im}(-\tilde{\varepsilon}^{-1}(\omega, \mathbf{q})) \approx \operatorname{Im}(-\tilde{\varepsilon}^{-1}(\omega, 0))$  the integration over  $q$  gives the well-known factor  $\ln \frac{\sqrt{E} + \sqrt{E - \hbar \omega}}{\sqrt{E} - \sqrt{E - \hbar \omega}} \approx \ln \frac{4E}{\hbar \omega}$ . The last approximation is correct if  $\hbar \omega \ll E$ .

The stopping power due to emission of phonons can be written in non-relativistic case as

$$\begin{aligned} & \left(-\frac{dE}{dx}\right)_{ph} \\ &= \frac{1}{\pi a_0 E} \int_0^{\min(\hbar \Omega_{\max}, E)} \frac{\hbar \omega}{1 - e^{-\hbar \omega/k_B T}} d(\hbar \omega) \operatorname{Im} \left( -\frac{1}{\varepsilon(\hbar \omega, 0)} \right) \ln \frac{\sqrt{E} + \sqrt{E - \hbar \omega}}{\sqrt{E} - \sqrt{E - \hbar \omega}} \\ & - \frac{1}{\pi a_0 E} \int_0^{\hbar \Omega_{\max}} \frac{\hbar \omega}{e^{\hbar \omega/k_B T} - 1} d(\hbar \omega) \operatorname{Im} \left( -\frac{1}{\varepsilon(\hbar \omega, 0)} \right) \ln \frac{\sqrt{E + \hbar \omega} + \sqrt{E}}{\sqrt{E + \hbar \omega} - \sqrt{E}}. \end{aligned} \quad (14)$$

We include phonon absorption and induced phonon emission processes in Eq. 14 (factors with Bose statistical factor,  $k_B T$  is the temperature in energy scale). We do not need to use such term in Eq. 12 since thermal energy  $k_B T \ll E_{ex}$ . The first term in Eq. 14 is greater than the second one for all energies  $E$  greater than  $\hbar \Omega_{\max}$ , and therefore the stopping power is positive for these energies. Using this formula one can estimate the production of vibrations and distortions of ionic system in the perturbed region generated by the passage of energetic electrons. In order to do this we can use the sum rules for electronic and vibrational parts of the energy loss function:

$$\int_{\Omega_{LO}}^{E/\hbar} \omega d\omega \operatorname{Im} \left( -\frac{1}{\varepsilon(\omega)} \right) = \frac{\pi}{2} \omega_{pl}^2(E) \equiv \frac{\pi e^2 N_{eff}(E)}{2 \varepsilon_0 m_0}, \quad (15)$$

$$\int_0^{\Omega_{LO}} \omega d\omega \text{Im} \left( -\frac{1}{\varepsilon(\omega)} \right) = \frac{\pi}{2} \Omega_{LO}^2. \quad (16)$$

Here  $\hbar\omega_{pl}$  is the plasmon energy, which can be expressed through effective concentration of electrons  $N_{eff}(E)$  involved in the transitions with the energy less than  $E$ . Therefore rough estimation of the ratio of energy loss channels for primary electron with kinetic energy well above plasmon energy  $\hbar\omega_{pl}$

$$\frac{(dE/dx)_{phonon}}{(dE/dx)_{e-h}} \approx \frac{\Omega_{LO}^2}{\omega_{pl}^2(E)} \approx \left( \frac{(10-100)\text{meV}}{(10-20)\text{eV}} \right)^2 \approx 10^{-6} - 10^{-4}. \quad (17)$$

Therefore for kinetic energies of electrons above the threshold for production of additional electronic excitations (which is close to  $E_{ex}$ ) we can neglect the phonon emission. So we can separate two stages of relaxation of electrons—cascade stage and thermalization stage.

In the following two sections we will discuss these results in more details.

### 3 First Stage—Cascade

The account for  $q$ -dependence of energy loss function in Eq. 12 can describe not only relatively low-energy electronic excitations and lattice vibrations (phonons) with small momentum  $\hbar\mathbf{q}$  but also much more rare events—impact production of fast electrons ( $\delta$ -electrons) and recoil ions (a very weak channel; we'll neglect it now).

The main problem is the calculation of the energy loss function  $\text{Im}(-\tilde{\varepsilon}^{-1}(\omega, \mathbf{q}))$ . The best way for calculation of energy loss function is the usage of contemporary band structure calculations. An example of such calculations is presented in [50]. Unfortunately it is difficult to use this type of calculation is wide energy region, and the calculation of matrix elements are not so exact as desirable. Here we use also approximate but much simpler way for estimation of  $\text{Im}(-\tilde{\varepsilon}^{-1}(\omega, \mathbf{q}))$  [20]. The steps of these calculations are the following:

1. First we calculate  $\varepsilon_2(\omega, 0) = \text{Im}(\tilde{\varepsilon}(\omega, 0))$  for zero transferred momentum. Here  $\varepsilon_2(\omega, 0)$  is calculated using the Evaluated Photon Data Library (EPDL97) databases [61] developed at the Lawrence Livermore National Laboratory. For the case of ionic crystals, this requires the following corrections: (i) modify the ionization energies of elements using the rigid shift of core level positions in order to obtain the correct ionization energies of shallow shells (a kind of the account for Madelung crystal potential) and (ii) change the population of the outer shells (e.g., for NaI we use the pure ionic model  $\text{Na}^+\text{I}^-$  with six electrons at 5p iodine valence shell and zero electrons at 3s sodium shell). The partial photon absorption cross sections for each shell  $j$  obtained from EPDL97 library are summed in order to obtain the imaginary part of dielectric permittivity

$$\varepsilon_2(\omega, 0) = \sum_j \varepsilon_2^j(\omega, 0). \quad (18)$$

2. The real part  $\varepsilon_1(\omega, 0)$  of  $\tilde{\varepsilon}(\omega, 0)$  is reconstructed using the Kramers–Krönig procedure. Knowing this function, we can calculate  $\text{Im}(-\tilde{\varepsilon}^{-1}(\omega, 0))$ . Then both  $\varepsilon_2(\omega, 0)$  and  $\text{Im}(-\tilde{\varepsilon}^{-1}(\omega, 0))$  functions are checked using the sum rules for the total number of electrons per unit crystal cell and for the value of low-frequency dielectric permittivity. Thus, we check that the resulting energy loss function shows the plasmon peak at the correct energy, and its intensity is also realistic.
3. Then we extrapolate the energy loss function for the case of nonzero  $\mathbf{q}$ . This method is equivalent to using the Generalized Oscillator Strength (GOS) approximation instead of Optical Oscillator Strength (OOS) [62–66]. We use the procedure based on the plane wave approximation of the final electron state. According to this approach, each partial dielectric permittivity function is extrapolated using the formula

$$\varepsilon_2(\omega, q) \approx \frac{m_0^{1/2}}{2\sqrt{2}\hbar^2\omega q} \sum_i \int_{E_i + \left(\sqrt{\hbar\omega - E_i} - \frac{\hbar q}{\sqrt{2m_0}}\right)^2}^{E_i + \left(\sqrt{\hbar\omega - E_i} + \frac{\hbar q}{\sqrt{2m_0}}\right)^2} \frac{\hbar\omega'}{(\hbar\omega' - E_i)^{1/2}} \varepsilon_2^i(\omega', 0) d(\hbar\omega'). \quad (19)$$

The result thus obtained for NaI is presented in Fig. 1.

Let us discuss the details of this electron loss function. First of all we introduce the variable  $E_q = \hbar^2 q^2 / 2m$  instead of  $q$ . In this case the limits of integration over this variable becomes  $(\sqrt{E} \pm \sqrt{E - \hbar\omega})^2$ . The maximal value of the upper integration limit equals to  $4E$  (for  $\hbar\omega = 0$ ). From simple kinematics considerations this case corresponds to the back scattering of the primary electron from the massive scattering center at  $\mathbf{q} = -2\mathbf{p}$ , and in this case the scattering angle is  $\pi$ . When  $E_q \approx E$ , the mean scattering angle for primary electron is about  $\pi/2$ . The scattering angle is small if  $E_q \ll E$ .

For high electron energies  $E > 1$  keV, most scattering events occur for small  $E_q$  due to two reasons: (1) the factor  $1/q$  in the integrand makes  $q$  small and therefore small  $E_q$  is more preferable for scattering and (2) Fig. 1 (lower panel) shows that the energy loss function rapidly decreases with increasing  $E_q$ . Therefore the primary electron trajectory deviates slightly at each scattering. The occurrence of scatterings with higher angular deviations of the trajectory is relatively rare. The Bethe ridge (see, e.g., [62]) of the energy loss function plays an important role in these rare scattering events. The Bethe ridge is the peak in the energy loss function near the line  $\hbar\omega = E_q$ . It is clearly shown in the bottom panel of Fig. 1 and describes the Mott scattering, if the exchange is taken into account) of the primary electron by quasi-free electrons. This scattering is the main reason of the creation of so-called  $\delta$ -rays. An additional reason

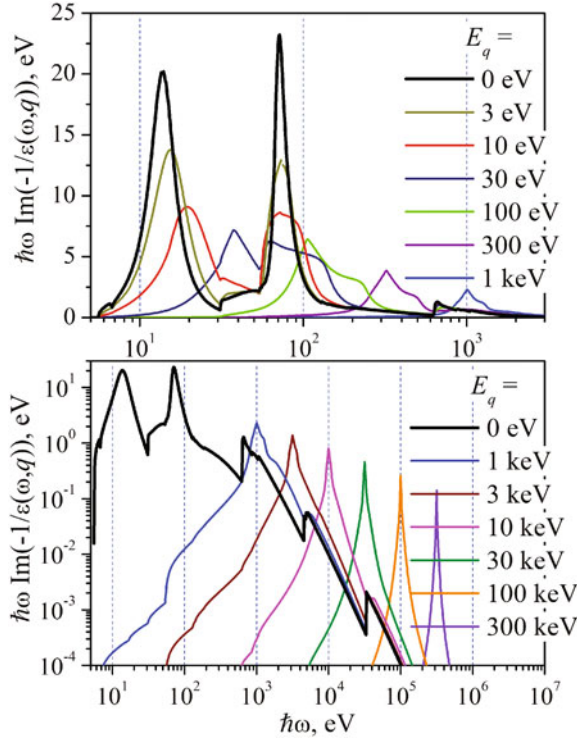


**Fig. 1.** Energy loss function  $\text{Im}(-\tilde{\epsilon}^{-1}(\omega, \mathbf{q}))$  multiplied by the energy loss  $\hbar\omega$  versus energy loss  $\hbar\omega$  for different values of  $q$  (here  $E_q = \hbar^2 q^2 / 2m_0$ ). Upper panel is for  $E_q \leq 1 \text{ keV}$  and lower panel is for  $E_q \geq 1 \text{ keV}$

for the creation of  $\delta$ -rays is the creation of high-energy Auger electrons followed after the ionization of K- and L-shells of heavy ions. This is again rather a rare process, as it can be seen from energy loss function presented in Fig. 1. These K- and L-shells can be filled also with the X-ray fluorescent photon emission, and the absorption of these photons creates high-energy electrons far enough from the main track. The creations of both deep core holes and  $\delta$ -rays are relatively rare effects, therefore the main part of energy is deposited in the crystal in the form of sequential low-angle scattering of the primary electron.

Energy loss function for NaI is characterized by many peculiarities since there are 22 core levels. Some of them have rather low ionization energy. Valence band (6 electrons per unit cell) form “plasmon” peak in 12–15 eV region. NaI energy loss function is characterized also by prominent peak due to ionization of 4dI core level at 60–80 eV region. The electrons from these levels (12 electrons per unit cell) form the second plasmon in this energy range. As usual, the energy loss function rapidly decrease with the increase of transferred energy  $\hbar\omega$ .

We can calculate the stopping power using this energy loss function and Eq. 9 (Fig. 2). This stopping power looks like common stopping power but it has two

maxima in low energy region due to two types of “plasmon” resonances described above. We also plot inverse value of inverse mean free path for ionizing particle  $1/\lambda(E)$ . Mean free path has about a standard form and reaches minimum at 20–30 eV region. In this region mean free path is less than the unit cell size.

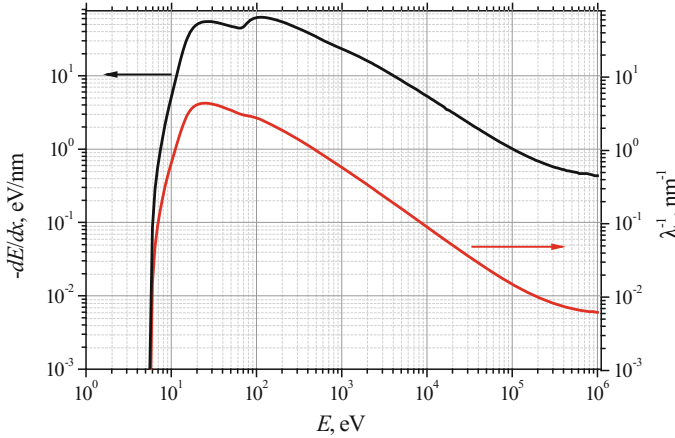


**Fig. 2.** Stopping power together with mean free path for electron in NaI calculated using energy loss function shown in Fig. 1

The ratio  $\langle \Delta E \rangle = (-dE/dx)/\lambda^{-1}$  gives the mean energy which the primary particle of energy  $E$  loses at each scattering. This mean energy is shown in the left panel of Fig. 3. Low energy electrons with energy just above forbidden gap energy  $E_g = 5.6$  eV for NaI, lose energy slightly exceeding  $E_g$ , whereas mean energy increases up to 70 eV for electrons with energy about 100 keV. This increase is explained by two reasons. Firstly, the energy of photoelectron ejected from core levels with energy  $E_i$ , increases with the increase of energy  $\hbar\omega$  transmitted to the media in a scattering ( $E_{kin} = \hbar\omega - E_i$ ). This energy increases till it reaches the ionization energy of the next core level (Fig. 3, right panel). Energy loss function shown in Fig. 1, shows that the fraction of high values of transferred energy  $\hbar\omega$  decreases rapidly with  $\hbar\omega$ . Nevertheless, the mean energy  $\langle \Delta E \rangle$  increases slowly with kinetic energy of primary electron. The ionization from deep core levels result in production of high-energy photoelectron and also high-energy Auger electrons after the relaxation of deep core level. These two kind of electrons behave like  $\delta$ -electrons and can produce their own tracks (branches of the main track of primary particle).

Presentation of imaginary part of dielectric permittivity as a sum of terms corresponding to transitions from different shells allows one to calculate partial mean free paths for excitation of different shells.

Figure 4 shows the total mean free path for scattering with production of new electronic excitations together with partial mean free paths, corresponding to ionization of different core shells (labeled in Fig. 4). We see that mean free path for production of a hole in K-shells of I is rather big and can be even longer than the range of the primary

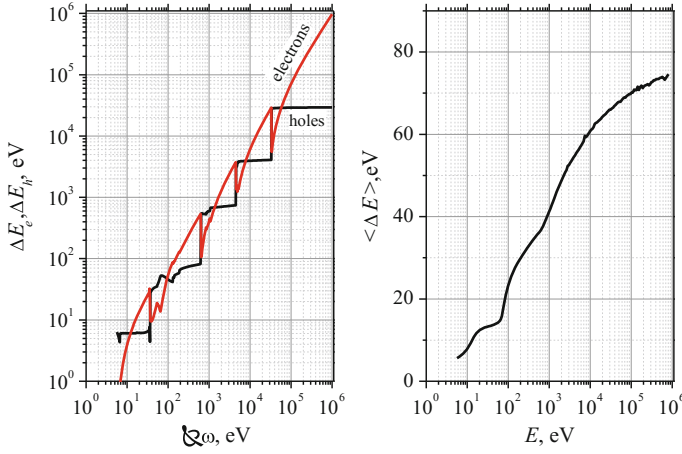


**Fig. 3.** Mean energy per scattering  $\langle \Delta E \rangle = (-dE/dx)/\lambda^{-1}$  as a function of the energy of primary particle for NaI (left panel) and mean energy passed to electron (light brown) and hole (blue) subsystems for energy transfer  $\hbar\omega$  in NaI (right panel)

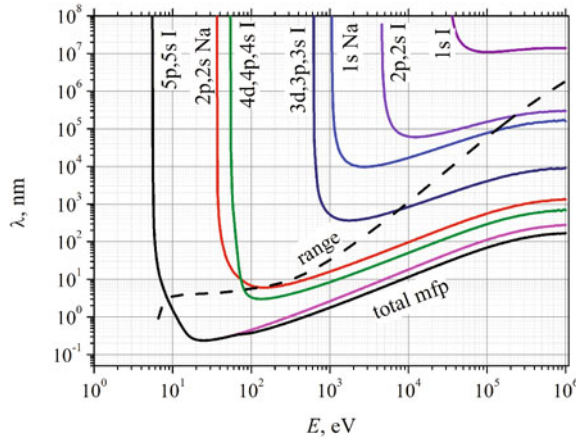


**Fig. 4.** Total (black) and partial mean free paths for production of excitations from different core levels in NaI. The range of electron with energy is also shown by dashed line

particle. This means that such core levels are ionized not in each track. On the contrary, holes are efficiently created at upper core levels (4dI, 2pNa).

The structure of energy losses result in strong fluctuation of energy deposit along the track. This effect is known as “Landau fluctuations”. Lev Landau calculated in [67] fluctuations of energy losses of ionizing particle passing through a thin layer of media, i.e. the fluctuation of energy deposit along the track. He calculated this distribution without account for core levels. For energy region below 1 meV core levels result in additional fluctuations. These fluctuations can be easily understand from comparison of

partial mean free paths and the total range of the ionizing particle. For instance, for 100 keV electron with range in NaI about 50  $\mu\text{m}$  valence electrons are excited each 100 nm, core levels with energies 60–80 eV are excited each 500–700 nm, 800 eV core is excited each 5 nm. Deeper levels are excited not at every track. After the excitation of core levels a hole is filled in with Auger process, resulting in creation of a cluster of holes in one or neighbor ions and few electrons with energies below the ionization energy of the corresponding core level. These electrons in turn produce several electron–hole pairs in the close vicinity of the initial core hole, since the mean free path for such electrons is about 1 nm. Therefore the track before the thermalization has a complicated structure and consists of individual electron–hole pairs and clusters of electrons and holes. Electrons have larger mean free path in comparison with hole's one, so these clusters consist of positive core with “halo” of electrons. The following thermalization can significantly change this distribution. This stage is discussed below.

The analogous cluster of excitation is created at the very end of each track of primary and energetic secondary excitations, since the last 1 keV of the energy of each energetic electron is released in the region with dimensions about 10 nm.

The points of creation of secondary excitations are positioned not strictly along the trajectory of the primary ionizing particle. In order to estimate at which distance from the trajectory secondary excitations are created, we have to return to formulas in the previous section. The electric field in the wake region of the ionizing particle are described by Eqs. 6 and 7. The energy of this field is distributed according to the equation

$$\pi \int_0^{\infty} r_{\perp} dr_{\perp} \left( E_{\parallel}^2(r_{\parallel}, r_{\perp}) + E_{\perp}^2(r_{\parallel}, r_{\perp}) \right). \quad (20)$$

In plasmon approximation (i.e. if energy loss function has only one peak at energy  $\hbar\omega_{pl}$ ) the integrals in Eqs. 6 and 7 can be estimated as

$$E_{\parallel}(r_{\parallel}, r_{\perp}, t) \sim -\frac{e\omega_{pl}^2}{2\pi\epsilon_0 v^2(E)} K_0 \left( \frac{\omega_{pl} \sqrt{r_{\perp}^2 + 4/q_{\max}^2}}{v(E)} \right) \cos(r_{\parallel}\omega_{pl}/v - \omega_{pl}t) \quad (21)$$

$$\begin{aligned} E_{\perp}(r_{\parallel}, r_{\perp}, t) &\sim \frac{e\omega_{pl}^2}{2\pi\epsilon_0 v^2(E)} \frac{r_{\perp}}{\sqrt{r_{\perp}^2 + 4/q_{\max}^2}} \\ &\times K_1 \left( \frac{\omega_{pl} \sqrt{r_{\perp}^2 + 4/q_{\max}^2}}{v(E)} \right) \sin(r_{\parallel}\omega_{pl}/v - \omega_{pl}t) \end{aligned} \quad (22)$$

Figure 5 shows the distribution of the wake electric field at the frequency corresponding to plasmon energy. The probability of the creation of electronic excitations with energy about plasmon energy  $\hbar\omega_{pl}$  is proportional to the energy of the field defined by Eq. 20. This picture shows that secondary excitations are created just along

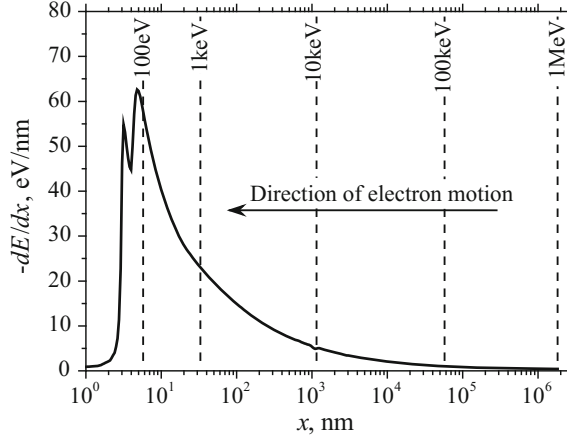


**Fig. 5.** Energy losses along the straitened electron track in NaI for different initial energies

the trajectory for low electron energy (0.2 nm for  $E = 30$  eV, 0.6 nm for  $E = 1$  keV), and are spreaded around the trajectory at mean distance about 3 nm for  $E = 100$  keV).

The deeper analysis of the distribution of electronic excitations shows that this distribution has some features of fractal structure with correlation dimension about 1.5–1.7.

The stopping power with the production of additional electron–hole pairs decreases to zero when the kinetic energy of moving charge approaches  $E_{ex}$ . In semiconductors Keldysh formula is often used,  $(dE/dx)_{e-h} \sim (E - E_{ex})^2$  (this formula is applicable for  $E < \hbar\omega_{pl}$ ) [68]. In crystals with strong excitonic effects the power is 1.5 instead of 2, but again the stopping power smoothly increases above the threshold [60]. Therefore in some energy region of kinetic energies above  $E_{ex}$  the inelastic scattering competes with the relaxation due to phonon emission, and the effective thresholds for the production of secondary excitations  $E_{th}^{(h)} > E_{ex}$ . At the end of the cascade stage all electrons and holes have kinetic energies smaller than  $E_{th}^{(h)}$  and therefore new electronic excitations cannot be produced any more. Electron and hole kinetic energies after the cascade stage can be described by distribution functions  $g_{e(h)}(E_{kin})$  from 0 to the energies slightly higher than  $E_{th}^{(h)}$ .

For the distribution of electrons over initial kinetic energy we will use analytical estimation which was obtained for the case of narrow valence band and uniform density of states in conduction band [28, 69].

$$g(E_{kin}) = \frac{1}{E_g} e^{-2C} \left[ 1 + (1 - E_{kin}/E_g) \int_0^\infty e^{(1-E_{kin}/E_g)z} (1 - e^{2\text{Ei}(-z)}) dz \right], \quad (23)$$

where  $C = 0.5772$  is the Euler constant. This distribution is plotted in Fig. 6. The main feature of this distribution is that the population of states with low kinetic energy is

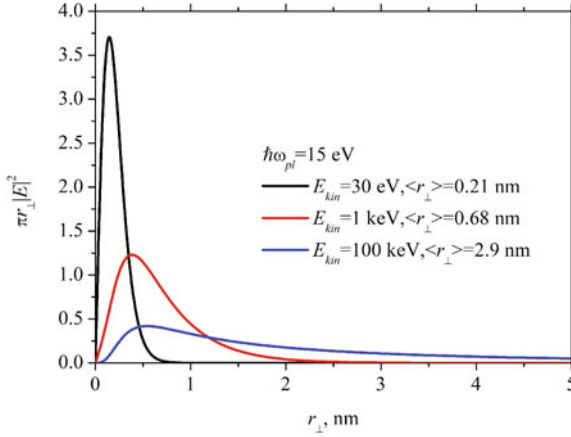


**Fig. 6.** Distribution of electric field of plasmons with energy  $\hbar\omega_{pl} = 15$  eV in transversal direction around the trajectory of an electron with different kinetic energies (30 eV, 1 keV and 100 keV)

about 5 times higher than the population of the electrons just below the threshold of inelastic scattering  $E_g$ . This qualitative result does not depend on the details of the scattering process, since electrons with energy  $E$  slightly above the threshold  $E_g$  can produce only low-energy secondaries in the range 0 to  $E - E_g$ , whereas electrons with kinetic energy well above  $E_g$  produce secondaries in much wider energy range. This general rule result in population of mainly low energy part of conduction band. About the same calculations were performed using Monte-Carlo approach [34, 35].

These distribution functions are supposed to be normalized:  $\int g_e(E_{kin}^e) dE_{kin}^e = 1$ ,  $\int g_h(E_{kin}^h) dE_{kin}^h = 1$ . The mean energy required for the creation of one electronic excitation is directly connected with this distribution:

$$E_{e-h} = E_g + \int E_{kin}^e g_e(E_{kin}^e) dE_{kin}^e + \int E_{kin}^h g_h(E_{kin}^h) dE_{kin}^h \equiv \beta E_g. \quad (24)$$

Therefore typical values of  $\beta$  are about 2 to 3 (see Fig. 3). The values of  $\beta$  can be larger than 3 for the crystals with wide valence bands and narrow forbidden gaps (in such crystals the relative difference between the threshold energies  $E_{th}^{e(h)}$  and  $E_g$  is large). On the contrary,  $\beta$  is less than 2 when the valence band is narrow. Moreover, some specific features of electronic structure can additionally reduce  $\beta$ . In [28] we demonstrated that the shift of the position of the uppermost core level in the series CsCl-CsBr-CsI relative to the threshold of Auger process can significantly modify  $g_e(E_{kin})$  and decrease  $\beta$ :  $\beta_{CsCl} > \beta_{CsBr} > \beta_{CsI}$  (see Fig. 7 illustrating this effect). A similar effect is connected with the position of the plasmon resonance and the threshold of multiplication of electronic excitations (see Fig. 8). The distribution of energy of secondary excitations is controlled by the energy loss function, and many electron-hole pairs are created with total energy about plasmon energy. If the plasmon

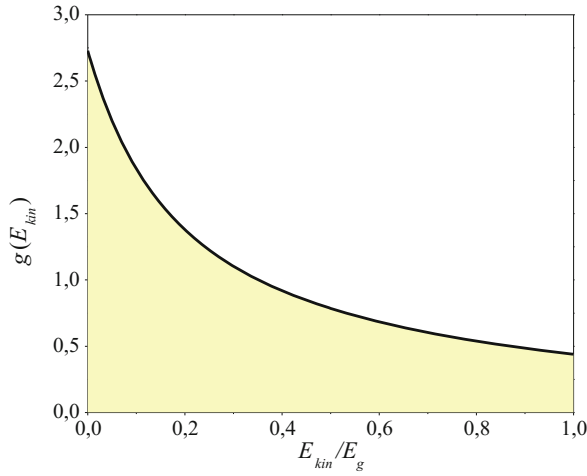


**Fig. 7.** Distribution of secondary electrons after the cascade in case of narrow valence band and uniform distribution of kinetic energy  $E_{kin}$  of secondary electrons between 0 and  $E - E_g$  after scattering of an electron with energy  $E$

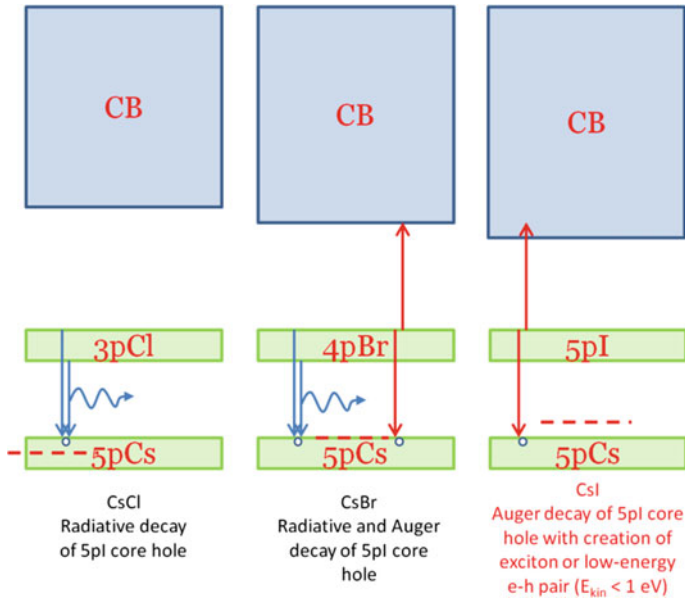


**Fig. 8.** Example of decrease of  $\beta_{CsCl} > \beta_{CsBr} > \beta_{CsI}$  in series CsCl-CsBr-CsI due to increasing possibility of Auger process of filling a hole in outermost core level

energy is higher than the electron threshold energy ( $\hbar\omega_{pl} > E_g + E_{th}^e$ ), most of these excitations in crystals with narrow valence bands could produce an additional low-energy electron-hole pair and thus reduce  $\beta$ . In the opposite case of  $\hbar\omega_{pl} < E_g + E_{th}^e$  most of the electrons from the plasmon resonance peak cannot produce additional pairs and cool down only by phonon emission. In this case  $\beta$  is also high (Fig. 9).

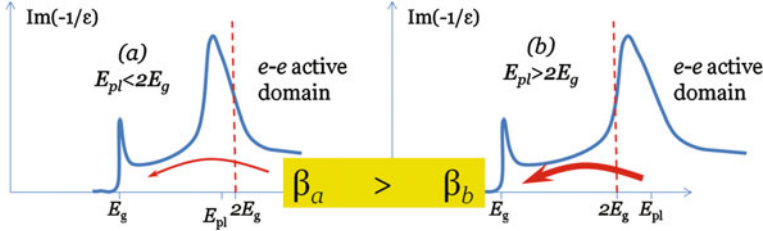


**Fig. 9.** Different relative positions of plasmon peak and threshold of electron-electron scattering. Left panel: Electron-hole pairs from plasmon peak region cannot produce additional electron-hole pairs and loose excess energy  $\hbar\omega_{pl} - E_g$  by emission of phonons. Right panel: Electron-hole pairs from plasmon peak region produce additional electron-hole pairs and loose excess energy  $\hbar\omega_{pl} - 2E_g$  by emission of phonons

## 4 Second Stage—Thermalization

At the thermalization (up to 10 ps) stage the interaction of moving charges with media is still described by the same formulas through the energy loss function, but at this stage the phonon channel (Eq. 14) is now the only channel of energy losses. During this stage all of the residual kinetic energy of electrons and holes will be transferred to phonons. The fraction  $1 - 1/\beta$  of the total deposited energy is emitted as phonons exactly at this thermalization stage, and this fraction can be large. Typical values of  $\beta$  are about 1.5–3, and therefore about 30–70% of energy is released as phonons. The main types of phonons, which are emitted in ionic crystals by electrons with high kinetic energy, are long-wavelength longitudinal optical (LO) phonons. The real part of dielectric permittivity in case of one LO phonon branch can be written as

$$\varepsilon^{-1}(\omega) = \varepsilon_{\infty}^{-1} + \frac{(\varepsilon_{\infty}^{-1} - \varepsilon_0^{-1})\Omega_{LO}^2}{\omega^2 - \Omega_{LO}^2} \quad (25)$$

where  $\varepsilon_0$  is static dielectric permittivity and  $\varepsilon_{\infty}$  is square of refraction index in the transparency region (for photon energies between  $\hbar\Omega_{LO}$  and  $E_{ex}$ ). It is convenient to introduce the effective dielectric permittivity

$$\varepsilon^* = (\varepsilon_\infty^{-1} - \varepsilon_0^{-1})^{-1}. \quad (26)$$

The energy loss function for LO phonon region becomes

$$\text{Im}\left(-\frac{1}{\tilde{\varepsilon}(\omega, \mathbf{q})}\right) = \frac{\pi\Omega_{LO}}{2\varepsilon^*} \delta(\omega - \Omega_{LO}). \quad (27)$$

It is worth to note that we can treat deformational acoustic phonon using this formalism by introduction energy loss function

$$\text{Im}\left(-\frac{1}{\tilde{\varepsilon}(\omega, \mathbf{q})}\right) = \frac{\pi\varepsilon_0\sigma_d^2q^3}{2c_{LA}e^2\rho} \delta(\omega - c_{LA}q) \quad (28)$$

where  $\sigma_d$  is deformation potential constant,  $c_{LA}$  is longitudinal sound velocity,  $\rho$  is the crystal density.

Substituting Eq. 27 into Eq. 14, it is possible to estimate the distance of thermalization of a carrier with effective mass  $m_e$  from initial kinetic energy  $E_{kin}$  down to energy of optical phonon  $\hbar\Omega_{LO}$  [36]:

$$\langle r^2 \rangle_{E_{kin} \rightarrow \hbar\Omega_{LO}} \approx \frac{8}{9} a_B^2 \left( \frac{\varepsilon^* m_0}{m_e} \right)^2 \tanh\left(\frac{\hbar\Omega_{LO}}{2k_B T}\right) \left( \frac{E_{kin}}{\hbar\Omega_{LO}} \right)^3 / \ln\left(\frac{4E_{kin}}{\hbar\Omega_{LO}}\right) \quad (29)$$

The evolution of  $\langle r^2 \rangle$  with decrease of the electron kinetic energy for two initial valued of initial kinetic energy (1 and 5 eV) is shown in Fig. 10 for four cases: (i) one LO phonon branch with rather high  $\hbar\Omega_{LO} = 0.1$  eV (the case of most crystals with light elements, e.g. oxygen or fluorine); (ii) one LO phonon branch with small  $\hbar\Omega_{LO} = 0.01$  eV (the case of CsI—a crystal with only heavy ions); (iii) the cases with two LO phonon modes, for which thermalization becomes faster. The thermalization from  $\hbar\Omega_{LO}$  to energies  $k_B T$  is due to interaction with acoustical phonons and the rate of energy relaxation also can be estimated by substituting Eq. 28 into Eq. 14.

The electrons with kinetic energy  $E_{kin}$  are therefore distributed in space after thermalization according to the following equation:

$$G(r) = \frac{3\sqrt{6}r^2}{\sqrt{\pi}(\langle r_e^2 \rangle + \langle r_h^2 \rangle)^{3/2}} \exp\left(-\frac{3r^2}{2(\langle r_e^2 \rangle + \langle r_h^2 \rangle)}\right) \quad (30)$$

Taking into account that kinetic energies of secondary electrons after the cascade stage are distributed from 0 to  $E_{ex}$  according to Eq. 23 (see Fig. 7), one have to average the distribution from Eq. 30 over kinetic energies of electrons and holes. Assuming that holes are generally less mobile than electrons, and the width of the valence band is typically less than  $E_{ex}$ , we can conclude that mostly electrons make input to the resulting separation of electrons and holes in geminate pairs. Similar distribution was obtained using Monte-Carlo technique [33].

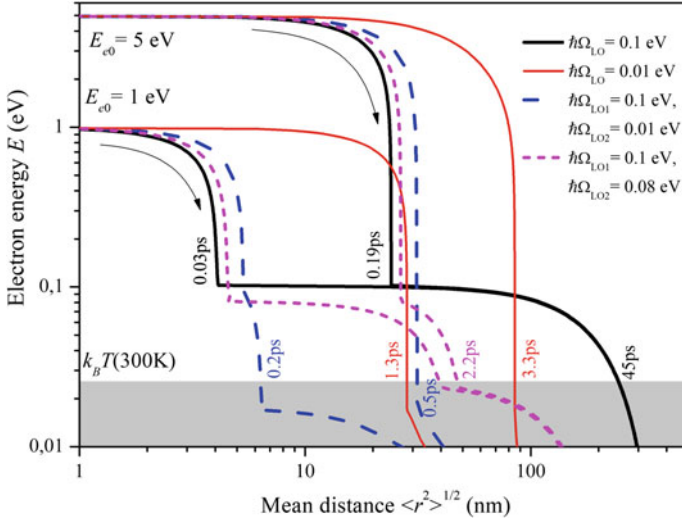


**Fig. 10.** Increase of the mean distance from the birthplace (horizontal axis) with decrease of energy (vertical axis) for different cases of one and two LO phonon branches. Arrows show direction of time. Parameters of simulation (effective masses, electron phonon strengths, etc.) are described in [36]. Thermalization times are mentioned by at the curves. Gray region correspond to thermalized carriers for 300 K. According to [28]

This distribution can be combined with the linear distribution of secondary excitations along the track shown in Fig. 5. The linear density of secondary excitation along the straitened track can be estimated as  $(-dE/dx)/(\beta E_g)$ . If we convolve this 1D distribution with 3D distribution of electrons and holes after the thermalization of geminate pairs (Fig. 11 and Eq. 30), we can calculate the distribution of concentration of excitations in the track region. This distribution of concentrations is shown in Fig. 12 for CsI at 300 K for different energies of ionizing particles. The plot shows the significant shift of the mean concentration of excitations when the energy of ionizing particle increases from 10 keV to 1 meV. Such distribution can be used for analysis of the last stage of scintillation processes (see the next section).

Above we discuss mainly properties and distribution of electronic excitations. Nevertheless, the destiny of phonons is also an interesting problem, especially for cryogenic application of scintillators. The kinetics of phonons in scintillators is not often discussed. Here we review some speculations of this problem [29]. Phonon mean free path is determined by phonon group velocity (for acoustical phonons it is equal to sound velocity at small phonon momentum, whereas for optical phonons it is usually much less than the sound velocity and is proportional to the phonon momentum). Lifetime of phonons is determined by the scattering processes, mainly phonon-phonon scattering due to anharmonicity (mainly splitting of phonon into two phonons, for instance low-momentum LO phonon is converted into two LA phonons with large opposite momenta). It is worth noting that normal processes result in conservation of total momentum, and therefore the main mechanism of dissipation is so-called umklapp

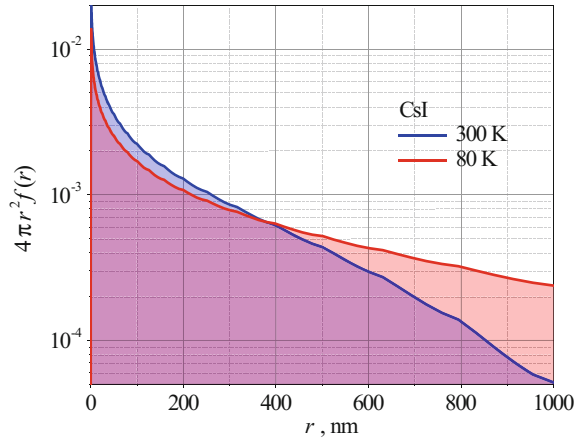


**Fig. 11.** Spatial distribution of thermalized secondary electrons over thermalization length for CsI in case of distribution of initial kinetic energy of secondaries according to Fig. 7 and Eq. 23. Curves are plotted for 300 and 80 K

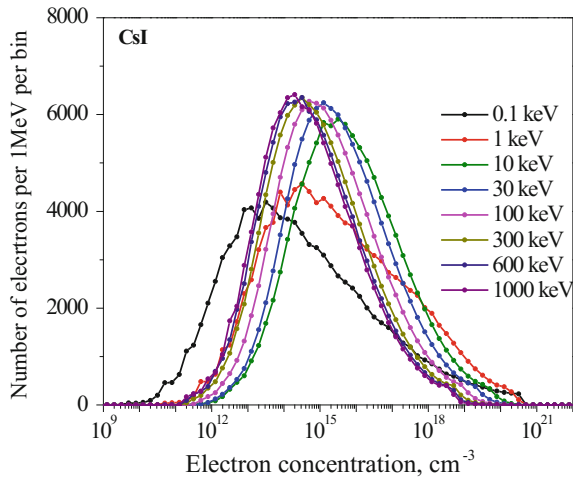


**Fig. 12.** Distribution of concentration of excitations in the track with account for thermalization for CsI at 300 K

processes, when the momentum can be preserved only with the account for additional basic vectors in the reciprocal space. Another important mechanism is phonon scattering on lattice defects and charge carriers. A typical phonon lifetime is about 1–100 ps, and the typical mean free path is about 1–100 nm (see, e.g. [70–72]). This mean free path is strongly temperature dependent, and at cryogenic temperatures the phonons are scattered mainly by crystal boundaries. These vibrationally excited regions can be especially important at the end of the track, where the density of secondary

electronic excitations is high, and along the whole track of heavy ionizing particles such as  $\alpha$ -particles or hadrons. We can estimate the electric fields induced in the media using Eqs. 6 and 7 (similar to Eqs. 21 and 22):

$$E_{\parallel}(r_{\parallel}, r_{\perp}, t) \sim -\frac{e\Omega_{LO}^2}{2\pi\epsilon_0\epsilon^*v^2(E)}K_0\left(\frac{\Omega_{LO}\sqrt{r_{\perp}^2 + 4/q_{\max}^2}}{v(E)}\right)\cos(r_{\parallel}\Omega_{LO}/v - \omega_{pi}t) \quad (31)$$

$$\begin{aligned} E_{\perp}(r_{\parallel}, r_{\perp}, t) &\sim \frac{e\Omega_{LO}^2}{2\pi\epsilon_0\epsilon^*v^2(E)}\frac{r_{\perp}}{\sqrt{r_{\perp}^2 + 4/q_{\max}^2}} \\ &\times K_1\left(\frac{\Omega_{LO}\sqrt{r_{\perp}^2 + 4/q_{\max}^2}}{v(E)}\right)\sin(r_{\parallel}\Omega_{LO}/v - \omega_{pi}t) \end{aligned} \quad (32)$$

The radius of this vibrationally excited region can be estimated as  $v/\Omega_{LO}$ , where  $v$  is the carrier velocity. For an electron with kinetic energy about 5 eV and  $\hbar\Omega_{LO} = 0.1$  eV this radius is about 8 nm. Typical spatial distribution of this electric field of LO vibrations directed along the track and perpendicular to the track for different phonon frequencies and different electron energies are shown in Fig. 13. These vibrations form the wake region produced by the travelling electron or hole. The total energy of the vibrations can be estimated using the expression:

$$2\pi\tilde{\epsilon}\frac{1}{2}\int_0^{\infty}\rho d\rho\left(E_z^2(z, \rho) + E_{\rho}^2(z, \rho)\right). \quad (33)$$

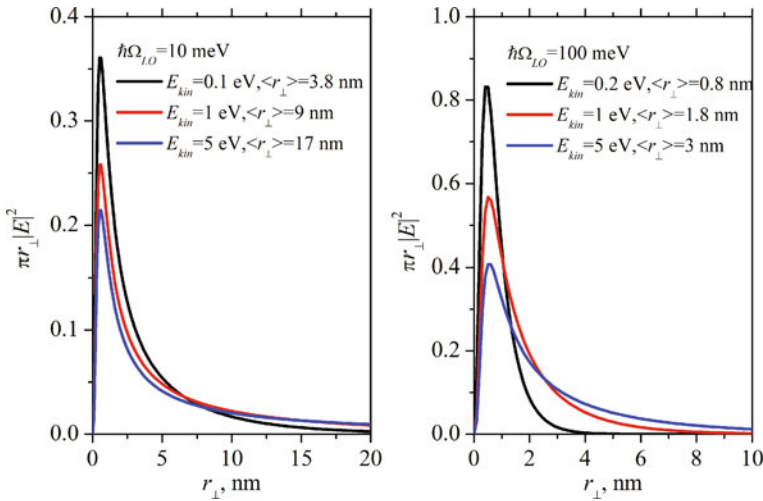


**Fig. 13.** Radial distribution of electric field in the wake region of a travelling particle for different electron kinetic energies and two values of phonon energy:  $\hbar\Omega_{LO} = 0.1$  eV (right panel) and  $\hbar\Omega_{LO} = 0.01$  eV (left panel)

This total energy should be equal to the phonon part of the energy losses

$$-\frac{dE}{dx} = \frac{\hbar^2 \Omega_{LO}^2}{2a_B e^* E} \ln \frac{\sqrt{E} + \sqrt{E - \hbar \Omega_{LO}}}{\sqrt{E} - \sqrt{E - \hbar \Omega_{LO}}}. \quad (34)$$

It should be noted that it is this electron–phonon interaction at these stages that controls the efficiency of intraband luminescence, which is regarded as one of the possible mechanisms of fast timing with the resolution of  $\sim 10$  ps [73].

Some parameters of the vibrational wake region produced by the travelling particle for two typical phonon energies are presented in Table 1. Here  $E_{kin}$  is the kinetic energy of the particle,  $\langle \rho \rangle$  is the mean radius of the vibrating region,  $\lambda_{LO}$  is the carrier mean free path with respect to LO phonon emission,  $\Delta E$  is the local deposit of vibrational energy along the track  $\left( \Delta E = \hbar \Omega_{LO} / \left( \pi \langle \rho \rangle^2 \lambda_{LO} \right) \right)$ , and the last column is the local deposit of this energy measured in Kelvin per  $\text{nm}^3$ .

**Table 1.** Some parameters of the wake region for different parts of thermalization trajectory

$\hbar \Omega_{LO}$ (eV)	$E_{kin}$ (eV)	$\langle \rho \rangle$ (nm)	$\lambda_{LO}$ (nm)	$\Delta E$ (meV/nm <sup>3</sup> )	$\Delta T$ (K/nm <sup>3</sup> )
0.1	0.2	0.75	0.6	70	814
0.1	1.0	1.8	1.5	12	142
0.1	5.0	3.0	5.0	2	24
0.01	0.1	3.8	1.4	0.5	6.6
0.01	1.0	9.0	8.9	0.03	0.46
0.01	5.0	17	35	0.005	0.06

In oxides and fluorides the typical value of  $\hbar \Omega_{LO} = 0.1$  eV. In this case the radius of the wake region is rather small for all kinetic energies from 0 to  $E_{ex}$ , and decreases from 3 nm for electrons with high kinetic energy (just below the threshold of inelastic scattering, which is about  $E_{ex}$ ), to less than 1 nm at the end of the thermalization path. The mean free path for LO phonon emission is rather low at the end of the trajectory (where kinetic energy is about few phonon energies). Therefore we can say that in crystals with such phonon energies the wake region is formed by rather compact phonon wavepackets, and overheating in this wake region is significant.

Phonon energy  $\hbar \Omega_{LO} = 0.01$  eV corresponds to iodide crystals. In this case the wake region is much wider, mean free path is longer, and therefore the local volume deposit of vibrational energy is much less than for the previous case. Therefore the temperature increase in the wake region is much less than for the case of oxides.

High energy deposit at the end of the thermalization trajectory does not mean that a carrier is stopped in this region with high temperature. In case of binary crystals the thermalization stage is splitted into two regions—relaxation with the emission of optical phonons is followed by the relaxation with the emission of acoustical phonons. The energy deposit along this part of the trajectory is small, and the total thermalization length can be rather long. Therefore a charge carrier can go away from the overheated region. This separation of the thermalization into two stages is typical only for binary

crystals. In crystals with complicated phonon structure the total thermalization is connected with different optical phonons, and therefore carriers could reach thermal energy in overheated zone.

Typical rates of  $LO \rightarrow LA + LA$  transformation is from 5 to 50 ps for GaAs [70]. Therefore the spatial expansion of the region with high intensity of optical vibrations occurs mainly in ballistic way over initial ten picoseconds. The spread velocity for acoustical phonons is equal to sound velocity (about  $5 \text{ nm/ps} = 5 \times 10^5 \text{ cm/s}$ ), whereas the velocity of wake region expansion is much less ( $v_{LO} = d\Omega_{LO}(q)/dq \ll c_{LA}$ , which is evident from the phonon energy dispersion law).

### 5 Third Stage—Interaction, Capture and Recombination

At the beginning of the last stage of scintillation process many thermalized excitations are present in the track region. This stage of interaction and recombination of excitations can be treated using kinetic (or rate) equations for concentration of different types of electronic excitations (electrons, holes, excitons, activators and defects etc.) (an example of the scheme of rate equations is shown in Fig. 14 and discussed in many papers, e.g., [43, 46, 47, 56, 57]). Such equations are widely used in chemical kinetics. Nevertheless the total number of reagents is rather small (about  $10^5$  for 1 meV ionizing particle), and statistics of these excitations is far from being equilibrium in space and time. Therefore such kinetic equations should be applied with some caution.

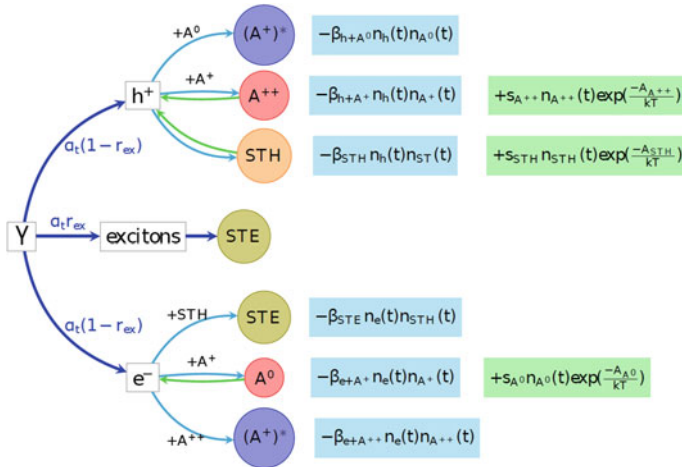


**Fig. 14.** Schematic representation of processes at the last stage of scintillation in crystals with activators [56]

These equations are studied deeply in order to simulate non-proportionality of scintillation yield and kinetics. Unfortunately such kinetic equations contain tens of parameters, most of them are known only with accuracy of the order of magnitude.

Therefore we will discuss here only the simplest model of interacting electrons, holes and excitons [21], which has all common features of much more elaborated models.

In most cases the diffusion of electrons, holes and electrons is not taken into account. The set of ordinary differential equations for these models includes linear, quadratic, cubic, bilinear and other higher order terms (see, e.g., [20, 22, 62]). The numerical solution of these equations does not allow detailed study of the dependence on parameters.

Some qualitative results can be found for analytically solvable set of equations. This model preserves the most important features of more complicated case, such as appearance of rise time for the response, fast initial stage of response and long emission components. The uniform distribution of excitations (excitons with concentration  $n_{ex}$  and holes and electrons with equal concentrations  $n_h = n_e$ ) is considered. No Auger recombination terms are included. The set of equations includes only second order terms and can be written as:

$$\begin{aligned}\frac{dn_{ex}(t)}{dt} &= -a_{ex}n_{ex}(t) - b_{ex-ex}n_{ex}^2(t) + g_{eh}n_e(t)n_h(t), \\ \frac{dn_e(t)}{dt} &= -(b_{eh} + g_{eh})n_e(t)n_h(t), \\ n_e(t) &= n_h(t).\end{aligned}\tag{35}$$

The equation for excitons describes radiative recombination with coefficient  $a_{ex} \equiv \tau_{ex}^{-1}$ ,  $\tau_{ex}$  is the exciton radiation time, quadratic term corresponding to exciton-exciton annihilation with rate coefficient  $b_{ex-ex}$ , and bi-linear term describing the recombination of electrons and holes into excitons with rate coefficient  $g_{eh}$ . For electrons and holes we take into account only bi-linear process, part of which result in production of excitons, and the rest one with coefficient  $b_{eh}$  describes non-radiative recombination of electrons and holes. Therefore this model includes one radiative channel (for excitons) and two quenching process—one due to non-radiative recombination of electrons and holes and another one due to exciton-exciton non-radiative quenching. The equations should be accomplished by initial conditions for total concentration of excitations created after thermalization  $n^0$  and the fraction of excitons  $f_{ex}$  among the excitations. Thus the concentration of excitons, electrons and holes at the beginning of this stage is  $n_{ex}(0) = n^0 f_{ex}$  and  $n_h(0) = n_e(0) = n^0(1 - f_{ex})$ .

This equation can be solved in terms of modified Bessel functions which is described in [21]. Several results of the decay curves for excitonic emission representing typical cases are shown below in Fig. 15 for different concentrations  $n^0$ . We can introduce the critical concentration  $n_{inter}$  as the concentration of excitons at which the rate of the exciton-exciton interaction equals to the radiative time:  $b_{ex-ex}n_{inter} = a_{ex}$ . For the examples the exciton-exciton interaction rate coefficient is taken to be equal to the total electron-hole recombination rate:  $b_{ex-ex} = b_{eh} + g_{eh}$ , and the recombination of a half of electron-hole pairs result the creation of an exciton/whereas another half annihilate non-radiatively:  $b_{eh} = g_{eh}$ . Two values of the initial branching ratio  $f_{ex}$  are taken. The value of  $f_{ex} = 0.8$  corresponds to the case when secondary excitations after cascade stage are mostly excitons and geminate electron-hole pairs. The lower value of

$f_{ex} = 0.05$  corresponds to the case that cascade and thermalization produce mostly separated electrons and holes (95%) which interact bi-molecularly. The curves in Fig. 15 are plotted both in linear scale of time (left panels) to show the initial rise time and quenching at initial stages, and in logarithmic scale (right panels) to represent long components.

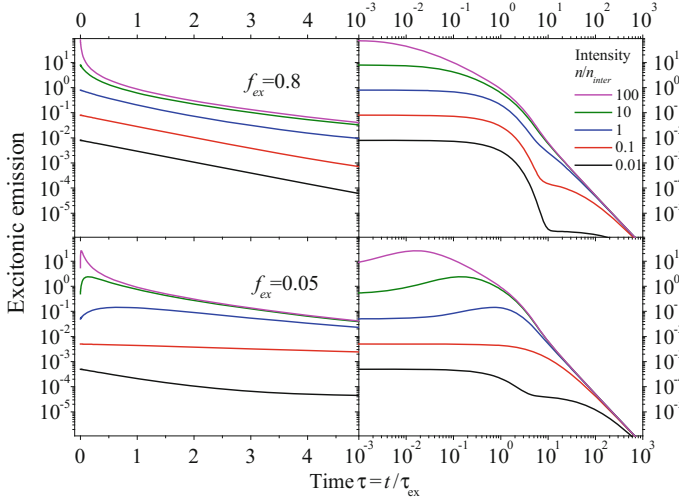


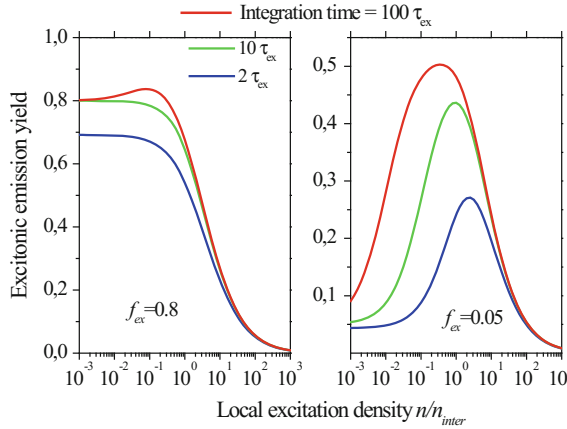
**Fig. 15.** Exciton decay kinetics for the model described by Eq. (35) (see [21]) for analytical form of these curves). Top panels correspond to creation of mainly excitons and geminate electron-hole pairs during previous stages, bottom panels, to creation of mainly separated electron-hole pairs. The exciton fraction  $f_{ex}$  and the dimensionless initial excitation concentration  $n^0/n_{inter}$  are shown in the plots

Log-Log graphs in right panels show that in both cases ( $f_{ex} = 0.8$  and  $f_{ex} = 0.05$ ) the long decay components are hyperbolic for times much longer than the exciton radiation time. The hyperbolic decay tail is observed even for low densities  $n \ll n_{inter}$ . Left panels show that in time domain from one exponential decay time  $\tau_{ex}$  to few  $\tau_{ex}$  the decay is about exponential for moderate excitation densities. High excitation intensities ( $n^0/n_{inter} = 10-100$ ) are characterized by non-exponential decay at initial stages. The rising part is appeared for creation of mainly separated electrons and holes ( $f_{ex} = 0.05$ ).

The scintillation yield is measured from the beginning of the signal to the definite ‘shaping’ time  $t_{sh}$ . For our model in homogeneous case this yield can be obtained using the following expression:

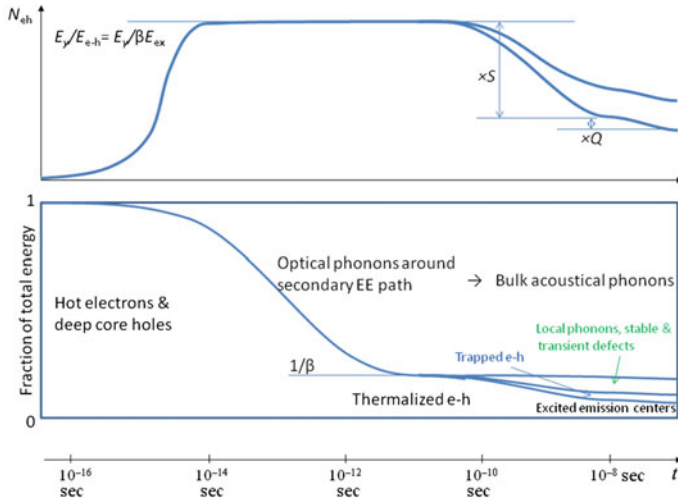
$$Y(n^0; t_{sh}) = \frac{1}{\tau_{ex} n^0} \int_0^{t_{sh}} n_{ex}(t; n^0) dt. \quad (36)$$

Figure 16 shows the dependence of the yield on the initial density of excitations. In case of creation of mainly excitons and geminate electron–hole pairs (left panel) the curves are characterized by the decrease of the yield for high concentrations. Only for high valued of shaping time a small hump of the yield is observed for moderate initial concentrations. On the contrary, the case when mainly separated electrons and holes are produced is characterized by prominent maximum of the yield for concentrations about  $n_{inter}$ . The shape of the yield curves strongly depends on integration time. Such dependence of the scintillator yield for alkali halide crystals on integration time was demonstrated for doped alkali halides [74]. These two types of the concentration dependence shown in left and right panels of Fig. 16 correspond to two types of non-proportionality curves: the right panel reflects the behavior of non-proportionality for binary alkali halide crystals, the left one is typical for many other crystals without hump in the non-proportionality curves. The result for  $f_{ex} = 0.8$  qualitatively corresponds to the case of good proportionality of the scintillation yield, whereas the result for  $f_{ex} = 0.05$ , to the alkali halide crystals. If we compare these curves with typical representation of non-proportionality curves, one have to note that high densities correspond to low energies of ionizing electron, whereas low densities correspond with high energy of the ionizing particle.



**Fig. 16.** Yield of exciton emission with shaping time  $t_{sh}$  from 2 to 100 exciton radiation decay time. The shaping time and the fraction of initially created excitons are labeled in the panels

Figures 15 and 16 correspond to uniform distribution of excitations. In order to pass to the energy of the primary ionizing particle, we have to weight these results with the distributions of concentration of excitations like those presented in Fig. 12. The detailed simulation of these curves are presented in numerous papers (see, e.g. [43, 46, 47, 56, 57]), but the qualitatively the non-proportionality yield and decay kinetics can be understood even for this simplified model.



**Fig. 17.** Evolution of the mean number of electronic excitations and fraction of electron and phonon channels. According to [29]

## 6 Conclusions

In the present paper we discuss systematically some important stages of the energy relaxation in scintillators, including creation of secondary excitations due to interaction of primary ionizing particle with media followed by the cascade of strongly inelastic scattering events with production of sequential secondaries—excitons and electron–hole pairs, thermalization stage with losing energy on phonon production, and interaction/recombination stage. Figure 17 shows the evolution of the mean number of electronic excitations and fraction of electron and phonon channels with time discussed in the previous sections.

Due to the lack of space we do not discuss many other methods of the investigation of processes in scintillators, like estimation of some properties using DFT calculations.

**Acknowledgements.** The author gratefully acknowledges financial support of the RF Ministry of Education and Science under the Agreement RFMEFI61614X0006.

## References

1. J.B. Birks, *Theory and Practice of Scintillation Counting* (Pergamon, New York, 1964), pp. 185–199
2. R.B. Murray, A. Meyer, Scintillation response of activated inorganic crystals to various charged particles. *Phys. Rev.* **112**, 815–826 (1961)
3. W.W. Moses, G.A. Bizarri, R.T. Williams, S.A. Payne, A.N. Vasil'ev, J. Singh, Q. Li, J.Q. Grim, W.S. Choong, The origins of scintillator non-proportionality. *IEEE Trans. Nucl. Sci.* **59**(5), 2038–2044 (2012)

4. A. Lempicki, A.J. Wojtowicz, E. Berman, Fundamental limits of scintillator performance. *Nucl. Instrum. Methods Phys. Res. A* **333**, 304–311 (1993)
5. P. Dorenbos, J.T.M. De Haas, C.W.E. Van Eijk, Non-proportionality in the scintillation response and the energy resolution obtainable with scintillation crystals. *IEEE Trans. Nucl. Sci.* **42**(6), 2190–2202 (1995)
6. B.D. Rooney, J.D. Valentine, Scintillator light yield nonproportionality: calculating photon response using measured electron response. *IEEE Trans. Nucl. Sci.* **44**(3), 509–516 (1997)
7. W. Mengesha, T.D. Taulbee, B.D. Rooney, J.D. Valentine, Light yield nonproportionality of CsI(Tl), CsI(Na), and YAP. *IEEE Trans. Nucl. Sci.* **45**(3), 456–461 (1998)
8. J.D. Valentine, B.D. Rooney, J. Li, The light yield nonproportionality component of scintillator energy resolution. *IEEE Trans. Nucl. Sci.* **45**(3), 512–517 (1998)
9. B.D. Rooney, J.D. Valentine, Benchmarking the Compton coincidence technique for measuring electron response non-proportionality in inorganic scintillators. *IEEE Trans. Nucl. Sci.* **43**, 1271–1276 (1996)
10. J.D. Valentine, B.D. Rooney, Design of a Compton spectrometer experiment for studying scintillator non-linearity and intrinsic energy resolution. *Nucl. Instrum. Methods Phys. Res. A Accel. Spectrom. Detect. Assoc. Equip.* **353**, 37–40 (1994)
11. W.S. Choong et al., Performance of a facility for measuring scintillator non-proportionality. *IEEE Trans. Nucl. Sci.* **NS-55**(3), 1073–1078 (2008)
12. W.S. Choong et al., Design of a facility for measuring scintillator nonproportionality. *IEEE Trans. Nucl. Sci.* **55**(3), 1753–1758 (2008)
13. M. Moszyński, A. Syntfeld-Kazuch, L. Swiderski, P. Sibczyński, M. Grodzicka et al., Energy resolution and slow components in undoped CsI crystals. *IEEE Trans. Nucl. Sci.* **63** (2), 459–466 (2016)
14. I.V. Khodyuk, J.T.M. de Haas, P. Dorenbos, Nonproportional response between 0.1–100 keV energy by means of highly monochromatic synchrotron X-rays. *IEEE Trans. Nucl. Sci.* **57**(3), 1175–1181 (2010)
15. I.V. Khodyuk, P. Dorenbos, Nonproportional response of LaBr:Ce and LaCl :Ce scintillators to synchrotron X-ray irradiation. *J. Phys. Condens. Matter* **22**, 485402 (2010)
16. I.V. Khodyuk, P.A. Rodnyi, P. Dorenbos, Nonproportional scintillation response of NaI:Tl to low energy X-ray photons and electrons. *J. Appl. Phys.* **107**, 113513-113513-8 (2010)
17. A. Belsky, I. Kamenskikh, A. Filippov, P. Martin, E. Meltchakov, S. Nannarone, A.N. Vasil'ev, Energy conversion of sub-KeV electronic excitations in inorganic scintillators, in *Proceedings of 8th International Conference on Inorganic Scintillators and their use in Scientific and Industrial Applications (SCINT2005)*, Kharkov, Ukraine, 2006, pp. 22–25
18. J.E. Jaffe, Energy nonlinearity in radiation detection materials: causes and consequences. *Nucl. Instrum. Methods Phys. Res. A* **580**, 1378–1382 (2007)
19. A.N. Vasil'ev, From luminescence non-linearity to scintillation nonproportionality. *IEEE Trans. Nucl. Sci.* **55**(3), 1054–1061 (2008)
20. G. Bizarri, W.W. Moses, J. Singh, A.N. Vasil'ev, R.T. Williams, An analytical model of nonproportional scintillator light yield in terms of recombination rates. *J. Appl. Phys.* **105**, 044507-1-15 (2009)
21. G. Bizarri, W.W. Moses, J. Singh, A.N. Vasil'ev, R.T. Williams, The role of different linear and non-linear channels of relaxation in scintillator non-proportionality. *J. Lumin.* **129**, 1790–1793 (2009)
22. G. Bizarri, N.J. Cherepy, W.S. Choong, G. Hull, W.W. Moses, S.A. Payne, J. Singh, J.D. Valentine, A.N. Vasil'ev, R.T. Williams, Progress in studying scintillator proportionality: phenomenological model. *IEEE Trans. Nucl. Sci.* **56**(4), 2313–2320 (2009)

23. S.A. Payne, N.J. Cherepy, G. Hull, J.D. Valentine, W.W. Moses, W.-S. Choong, Nonproportionality of scintillator detectors: theory and experiment. *IEEE Trans. Nucl. Sci.* **56**, 2506–2512 (2009)
24. S.A. Payne, W.W. Moses, S. Sheets, L. Ahle, N.J. Cherepy, B. Sturm, S. Dazeley, G. Bizarri, W.-S. Choong, Nonproportionality of scintillator detectors: theory and experiment II. *IEEE Trans. Nucl. Sci.* **58**, 3392–3402 (2011)
25. S.A. Payne, S. Hunter, L. Ahle, N.J. Cherepy, E. Swanberg, Nonproportionality of scintillator detectors. III. Temperature dependence studies. *IEEE Trans. Nucl. Sci.* **61**(5), 2771–2777 (2014)
26. S.A. Payne, Nonproportionality of scintillator detectors. IV. Resolution contribution from delta-rays. *IEEE Trans. Nucl. Sci.* **62**(1), 372–380 (2015)
27. P.R. Beck, S.A. Payne, S. Hunter, L. Ahle, N.J. Cherepy, E.L. Swanberg, Nonproportionality of scintillator detectors. V. Comparing the gamma and electron response. *IEEE Trans. Nucl. Sci.* **62**(3), 1429–1436 (2015)
28. A.N. Vasil'ev, A.V. Gektin, Multiscale approach to estimation of scintillation characteristics. *IEEE Trans. Nucl. Sci.* **61**, 235–245 (2014)
29. A. Gektin, A. Vasil'ev, Scintillation, phonon and defect channel balance; the sources for fundamental yield increase. *Funct. Mater.* **23**(2), 183–190 (2016)
30. A.N. Vasil'ev, I.A. Markov, A.S. Zakharov, Usage of polarization approximation for the estimation of scintillator intrinsic energy resolution. *Radiat. Meas.* **45**, 258–261 (2010)
31. S. Agostinelliae, J. Allisonas, K. Amakoe et al., Geant4—a simulation toolkit. *Nucl. Instrum. Methods Phys. Res. A* **506**, 250–303 (2003)
32. J. Allison, K. Amako, J. Apostolakis et al., Geant4 developments and applications. *IEEE Trans. Nucl. Sci.* **53**(1), 270–278 (2006)
33. F. Gao, Y. Xie, S. Kerisit, L.W. Campbell, W.J. Weber, Yield, variance and spatial distribution of electron–hole pairs in CsI. *Nucl. Instrum. Methods Phys. Res. A* **652**, 564–567 (2011)
34. Z. Wang, Y. Xie, B.D. Cannon, L.W. Campbell, F. Gao, S. Kerisit, Computer simulation of electron thermalization in CsI and CsI(Tl). *J. Appl. Phys.* **110**, 064903 (2011)
35. Z. Wang, Y. Xie, L.W. Campbell, F. Gao, S. Kerisit, Monte Carlo simulations of electron thermalization in alkali iodide and alkaline-earth fluoride scintillators. *J. Appl. Phys.* **112**, 014906 (2012)
36. R. Kirkin, V.V. Mikhailin, A.N. Vasil'ev, Recombination of correlated electron–hole pairs with account of hot capture with emission of optical phonons. *IEEE Trans. Nucl. Sci.* **59**(5), 2057–2064 (2012)
37. A. Belsky, K. Ivanovskikh, A. Vasil'ev, M.F. Joubert, C. Dujardin, Estimation of the electron thermalization length in ionic materials. *J. Phys. Chem. Lett.* **4**, 3534–3538 (2013)
38. M.P. Prange, L.W. Campbell, D. Wu, F. Gao, S. Kerisit, Calculation of energy relaxation rates of fast particles by phonons in crystals. *Phys. Rev. B* **91**, 104305 (2015)
39. W. Setyawan, R.M. Gaume, R.S. Feigelson, S. Curtarolo, Comparative study of nonproportionality and electronic band structures features in scintillator materials. *IEEE Trans. Nucl. Sci.* **56**(5), 2989–2996 (2009)
40. A. Canning, R. Boutchko, A. Chaudhry, S.E. Derenzo, First-principles studies and predictions of scintillation in Ce-doped materials. *IEEE Trans. Nucl. Sci.* **56**(3), 944–948 (2009)
41. A. Canning, A. Chaudhry, R. Boutchko, N. Grønbech-Jensen, First-principles study of luminescence in Ce-doped inorganic scintillators. *Phys. Rev. B Condens. Matter.* **83**, 125115 1–125115 12 (2011)

42. H. Huang, Q. Li, X. Lu, Y. Qian, Y. Wu, R.T. Williams, Role of hot electron transport in scintillators: a theoretical study. *Phys. Status Solidi (RRL)-Rapid Res. Lett.* **10**(10), 762–768 (2016)
43. X. Lu, Q. Li, G.A. Bizarri, K. Yang, M.R. Mayhugh, P.R. Menge, R.T. Williams, Coupled rate and transport equations modeling proportionality of light yield in high-energy electron tracks: CsI at 295 K and 100 K; CsI: Tl at 295 K. *Phys. Rev. B* **92**(11), 115207 (2015)
44. J.Q. Grim, Q. Li, K.B. Ucer, A. Burger, G.A. Bizarri, W.W. Moses, R.T. Williams, The roles of thermalized and hot carrier diffusion in determining light yield and proportionality of scintillators. *Phys. Status Solidi (a)* **209**(12), 2421–2426 (2012)
45. Q. Li, J.Q. Grim, K.B. Ucer, A. Burger, G.A. Bizarri, W.W. Moses, R.T. Williams, Host structure dependence of light yield and proportionality in scintillators in terms of hot and thermalized carrier transport. *Phys. Status Solidi (RRL)-Rapid Res. Lett.* **6**(8), 346–348 (2012)
46. Q. Li, J.Q. Grim, R.T. Williams, G.A. Bizarri, W.W. Moses, A transport-based model of material trends in nonproportionality of scintillators. *J. Appl. Phys.* **109**(12), 123716 (2011)
47. R.T. Williams, J.Q. Grim, Q. Li, K.B. Ucer, W.W. Moses, Excitation density, diffusion-drift, and proportionality in scintillators. *Phys. Status Solidi (b)* **248**(2), 426–438 (2011)
48. S.A. Gorbunov, P.N. Terekhin, N.A. Medvedev, A.E. Volkov, Combined model of the material excitation and relaxation in swift heavy ion tracks. *Nucl. Instrum. Methods Phys. Res. B* **315**, 173–178 (2013)
49. A. Kozorezov, J.K. Wigmore, A. Owens, Picosecond dynamics of hot carriers and phonons and scintillator nonproportionality. *J. Appl. Phys.* **112**, 053709 (2012)
50. L.W. Campbell, F. Gao, Excited state electronic properties of sodium iodide and cesium iodide. *J. Lumin.* **137**, 121–131 (2013)
51. S. Kerisit, Z. Wang, R.T. Williams, J.Q. Grim, F. Gao, Kinetic Monte Carlo simulations of scintillation processes in NaI (Tl). *IEEE Trans. Nucl. Sci.* **61**(2), 860–869 (2014)
52. Z. Wang, R.T. Williams, J.Q. Grim, F. Gao, S. Kerisit, Kinetic Monte Carlo simulations of excitation density dependent scintillation in CsI and CsI (Tl). *Phys. Status Solidi (b)* **250**(8), 1532–1540 (2013)
53. M. Kirm, V. Nagirnyi, E. Feldbach, M. De Grazia, B. Carre, H. Merdji, S. Guizard, G. Geoffroy, J. Gaudin, N. Fedorov, P. Martin, A. Vasil'ev, A. Belsky, Exciton-exciton interactions in CdWO<sub>4</sub> irradiated by intense femtosecond vacuum ultraviolet pulses. *Phys. Rev. B* **79**, 233103 (2009)
54. N. Fedorov, A. Belsky, E. Constant, D. Descamps, P. Martin, A.N. Vasil'ev, Quenching of excitonic luminescence of alkaline earth fluorides excited by VUV harmonics of femtosecond laser. *J. Lumin.* **129**, 1813–1816 (2009)
55. J.Q. Grim, K.B. Ucer, A. Burger, P. Bhattacharya, E. Tupitsyn, E. Rowe et al., Nonlinear quenching of densely excited states in wide-gap solids. *Phys. Rev. B* **87**(12), 125117 (2013)
56. S. Gridin, A. Belsky, C. Dujardin, A. Gektin, N. Shiran, A. Vasil'ev, Kinetic model of energy relaxation in CsI: A (A = Tl and In) scintillators. *J. Phys. Chem. C* **119**, 20578–20590 (2015)
57. S. Gridin, A.N. Vasil'ev, A. Belsky, N. Shiran, A. Gektin, Excitonic and activator recombination channels in binary halide scintillation crystals. *Phys. Status Solidi B* **251**, 942–949 (2014)
58. L.D. Landau, E.M. Lifshitz, *The Classical Theory of Fields* (Volume 2 of A Course of Theoretical Physics) (Pergamon Press, UK, 1971)
59. N.P. Kalashnikov, V.S. Remizovich, M.I. Ryazanov, *Collisions of Fast Charged Particles in Solids* (Gordon and Breach, New York, 1985)

60. A.N. Vasil'ev, Y. Fang, V.V. Mikhailin, Impact production of secondary electronic excitations in insulators: multiple-parabolic-branch band model. *Phys. Rev. B* **60**, 5340–5347 (1999)
61. D.E. Cullen, J.H. Hubbell, L. Kissel, EPDL97, the evaluated photon data library, '97 version, Lawrence Livermore National Laboratory. UCRL-50400 **6**(5) (1997)
62. M. Inokuti, Inelastic collisions of fast charged particles with atoms and molecules—the bethe theory revisited. *Rev. Mod. Phys.* **43**, 297 (1971)
63. R. Mayol, F. Salvat, Cross sections for K-shell ionisation by electron impact. *J. Phys. B* **23**, 2117 (1990)
64. J.C. Ashley, Simple model for electron inelastic mean free paths: application to condensed organic materials. *J. Electron Spectrosc. Relat. Phenom.* **28**, 177 (1982)
65. J.C. Ashley, Interaction of low-energy electrons with condensed matter: stopping powers and inelastic mean free paths from optical data. *J. Electron Spectrosc. Relat. Phenom.* **46**, 199 (1988)
66. D.R. Penn, Electron mean-free-path calculations using a model dielectric function. *Phys. Rev. B* **35**, 482 (1987)
67. L.D. Landau, On the energy loss of fast particles by ionization. *J. Exp. Phys. (USSR)* **8**, 201–205 (1944), in *Collected Papers of L.D. Landau*, ed. by D. Ter Haar (Gordon and Breach Science Publishers, NY/London/Paris, 1965)
68. L.V. Keldysh, Concerning the theory of impact ionization in semiconductors. *Sov. Phys. JETP* **21**, 1135 (1965)
69. A.N. Vasil'ev, V.V. Mikhailin, The role of relaxation through phonon emission in cascade process of multiplication of electronic excitations generated by X-ray quantum. *Bull. Acad. Sci. USSR. Phys. Ser.* **50**(3), 113–116 (1986)
70. T. Luo, J. Garg, J. Shiomi, K. Esfarjani, G. Chen, Gallium arsenide thermal conductivity and optical phonon relaxation times from first-principles calculations. *Europhys. Lett.* **101**, 16001 (2013)
71. T. Feng, X. Ruan, Prediction of spectral phonon mean free path and thermal conductivity with applications to thermoelectrics and thermal management: a review. *J. Nanomater.* **2014**, 206370 (2014)
72. J.P. Freedman, J.H. Leach, E.A. Preble, Z. Sitar, R.F. Davis, Universal phonon mean free path spectra in crystalline semiconductors at high temperature. *Sci. Rep.* **3**, 2963 (2013)
73. P. Lecoq, M. Korzhik, A. Vasil'ev, Can transient phenomena help improving time resolution in scintillators. *IEEE Trans. Nucl. Sci.* **61**, 229 (2014)
74. M. Moszyński, A. Nassalski, A. Syntfeld-Każuch, Ł. Świdorski, T. Szczęśniak, Energy resolution of scintillation detectors—new observations. *IEEE Trans. Nucl. Sci.* **55**, 1062 (2008)

Engineering of Scintillation Materials and Radiation  
Technologies

Proceedings of ISMART 2016

Korzhik, M.; Gektin, A. (Eds.)

2017, XII, 339 p. 233 illus., 93 illus. in color., Hardcover

ISBN: 978-3-319-68464-2